Asociación Argentina
de Mecánica Computacional

Mecánica Computacional Vol XXXIV, págs. 655-679 (artículo completo)
Sebastián Giusti, Martín Pucheta y Mario Storti (Eds.)
Córdoba, 8-11 Noviembre 2016

NON-LINEAR SECTIONAL ANALYSIS OF REINFORCED CONCRETE MEMBERS

Mauro Poliotti[a], Oscar Möller[a,b], Juan P. Ascheri[a] and Pablo L. Sierra[a]

[a]*Instituto de Mecánica Aplicada y Estructuras (IMAE),Facultad de Cs.Ex., Ingeniería y Agrimensura, Universidad Nacional de Rosario, Riobamba y Berutti, 2000 Rosario, Argentina, poliotti@fceia.unr.edu.ar, http://www.imae.fceia.unr.edu.ar*

[b]*Consejo de Investigaciones (CIUNR), Universidad Nacional de Rosario, Maipú 1065, 2000 Rosario, Argentina, http://www.unr.edu.ar*

Keywords: Reinforced Concrete Sectional Analysis, Plastic-Damage Model, Unified Non-linear Library.

Abstract. In the most general case 3D reinforced concrete frame are subjected to complex load states that lead to a combination of axial and shear forces, torsion and bending moments on each frame element. Material non-linearity produce an anisotropic behavior that leads to the coupling between all the six efforts. In this work a sectional model and code for non-linear analysis of reinforced concrete member developed by other authors is presented. This model is able to reproduce the complex coupled behavior of a reinforced concrete section and can be used as a constitutive equation on each integration point of any flexibility based frame model. In order to contribute to the improvement of the sectional model and the implemented code, a plastic-damage model based in plasticity theory and fracture-energy damage concept is presented and implemented to model concrete behavior. Also a unified library of non-linear solver schemes is presented and implemented to allow the code to deal with highly non-linear problems. Finally the code with the new constitutive law and non-linear library is tested trough a series of examples showing the capabilities of the sectional analysis.

1 INTRODUCTION

Reinforced concrete frame structures can be subjected to complex dynamic or static load states that lead to a combination of axial and shear forces, torsion and bending moments on each frame element. Non-linear behavior of concrete and steel, specially cracking on concrete and yielding of reinforcement produce an anisotropic response that cause the coupling between all the six efforts on the three-dimensional case. In order to trace accurately the response of such structures the interaction of all the efforts must be taken into account.

Traditionally to capture this phenomenon, complex 2D or 3D finite element analysis was made, but its high computational cost is not suitable for usual engineering practice. Beam elements are widely spread between structural engineers because of their robustness and the time savings in modeling and post-processing steps of analysis, also because beam models are more related to engineers reasoning and to design process prescribed by most of current construction codes than a full 3D analysis.

Nevertheless most of beam models fail to reproduce the interaction between normal and tangential efforts. One family of elements is worth to be mentioned from the wide range of beam models that exists nowadays, these are fiber beam models (Taucer et al., 1991; Möller et al., 2009; Poliotti et al., 2013) which are able to reproduce the interaction between axial force and bending moments, in order to do this on each integration point of the element they discretize the cross section of the beam into concrete and steel fibers each one with his uniaxial constitutive law, and after calculating the elongation of each fiber through a proper kinematic hypothesis (Navier-Bernoulli) they can calculate the force contribution of each fiber and the efforts on the cross section see Fig. (1). But it is because the inter-fiber equilibrium is neglected that they cannot reproduce the interaction between normal and tangential efforts.

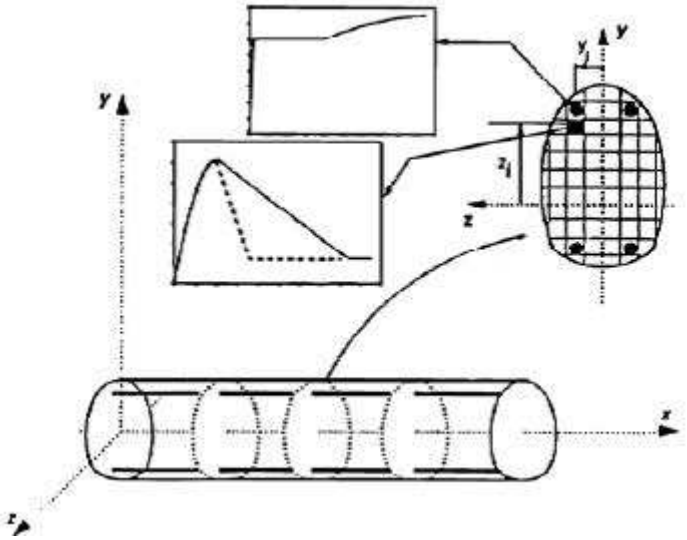

Figure 1: Fiber beam model

In order to account the interaction of all possible efforts and with the section analysis introduced by the fiber models as a basis, Bairán (2005); Bairán and Marí (2006a,b) introduced a new model for sectional analysis that reproduces coupling of normal and tangential efforts. This model was implemented on a finite element environment called TINSA (Total Interaction Nonlinear Section Analysis). This model can be used as a constitutive equation for general beam elements at their integration points.

First in this work the study of the sectional model TINSA is presented. Then, in order to contribute to the improvement of the robustness of the finite element code, a coupled plastic-damage constitutive law for concrete based in the plasticity theory with hardening variables defined by the fracture-energy damage concept first introduced by Lubliner et al. (1989) and then extended by Lee and Fenves (1998) is introduced and implemented in the FE code. Also a unified library of nonlinear solvers including load, displacements, arc-length and work control methods introduced by Leon et al. (2011) is presented and implemented in order to allow the FE code to deal with highly nonlinear problems. Application examples and study cases are presented in order to test the sectional model with the constitutive law and the nonlinear library. Finally conclusion and further developments are summarized.

2 SECTIONAL MODEL - TINSA

In the following the analytic model and finite code TINSA are presented. This model considers the inter-fiber equilibrium explicitly leading to the interaction between tangential and axial efforts and constitutes a powerful tool to study the behavior of cross sections of beams under complex load states. The model is more expensive in a computational point of view that classical beams elements, but it can reproduce 3D complex states without the cost of a full 3D analysis.

2.1 General assumptions

The domain that's considered in the following formulation is an arbitrary shaped cross section belonging to a beam-column element. The sections is defined in the y-z plane with normal x parallel to the beam axis. The cross section is intersected by the beam axis in a point defined by the vector $\mathbf{r}_0$. The generalized displacements of the section at this point are six: three rigid body translations (u_0, v_0, w_0) and three rigid body rotations $(\theta_x, \theta_y, \theta_z)$. See Fig. (2).

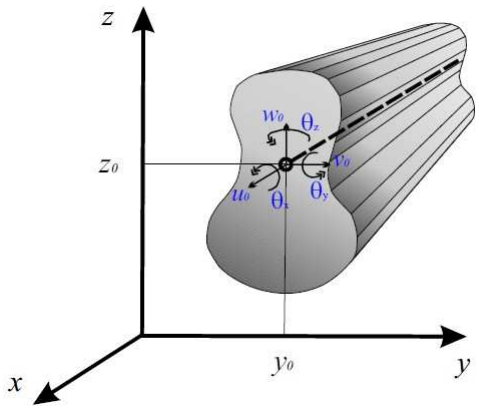

Figure 2: Domain, local axis and generalized displacements

The main assumption of the sectional model is that the displacement field at the cross section can be calculated by superposition of two orthogonal fields, a "plane section" displacement field consistent with Navier-Bernoulli's hypothesis $\mathbf{u}^{PS}$, and a "warping-distortion" displacement field which can reproduce out of plane warping and section's change of shape $\mathbf{u}^{W}$. See Fig. (3).

$$\mathbf{u} = \mathbf{u}^{PS} + \mathbf{u}^{W} \tag{1}$$

As small perturbations hypothesis is assumed, the same decomposition can be straightforward made with strains.

$$\boldsymbol{\varepsilon} = \mathbf{L}\mathbf{u} = \mathbf{L}\mathbf{u}^{PS} + \mathbf{L}\mathbf{u}^{W} = \boldsymbol{\varepsilon}^{PS} + \boldsymbol{\varepsilon}^{W} \tag{2}$$

Where $\mathbf{L}$ is the linear operator:

$$\begin{aligned}\mathbf{L} = \mathbf{L}_x + \mathbf{L}_{yz} =& \frac{\partial}{\partial x}\mathbf{E}_x + \mathbf{L}_{yz} \\ =& \begin{bmatrix} \frac{\partial}{\partial x} & 0 & 0 & 0 & 0 & 0 \\ 0 & 0 & 0 & \frac{\partial}{\partial x} & 0 & 0 \\ 0 & 0 & 0 & 0 & \frac{\partial}{\partial x} & 0 \end{bmatrix}^T + \begin{bmatrix} 0 & 0 & 0 & \frac{\partial}{\partial y} & \frac{\partial}{\partial z} & 0 \\ 0 & \frac{\partial}{\partial y} & 0 & 0 & 0 & \frac{\partial}{\partial z} \\ 0 & 0 & \frac{\partial}{\partial z} & 0 & 0 & \frac{\partial}{\partial y} \end{bmatrix}^T\end{aligned} \tag{3}$$

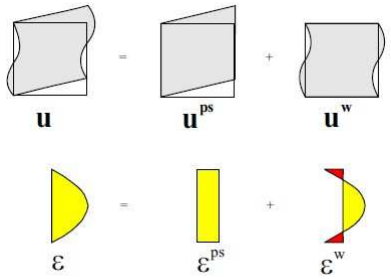

Figure 3: Plane Section - Warping Distortion decomposition

The same decomposition can be made with stresses if the material is linear nevertheless if the material is nonlinear it can be proved that this decomposition is valid in an incremental way.

$$\dot{\boldsymbol{\sigma}} = \dot{\boldsymbol{\sigma}}^{PS} + \dot{\boldsymbol{\sigma}}^{W} \tag{4}$$

2.2 Navier-Bernoulli's theory. Plane section displacement field

The basic assumption of NB beam theory is that plane sections remain plane and orthogonal to beams axis after deformation. This kinematic hypothesis can be written as follows:

$$v_0' = \theta_z; w_0' = -\theta_y \tag{5}$$

The displacement field is defined only by the plane section field being the warping distortion displacement field null $\mathbf{u}^W = 0$. The vector of plane section displacement is computed using the generalized displacements of the section $\mathbf{u}_s(x)$.

$$\boldsymbol{u}^{PS}(x,y,z) = \boldsymbol{N}^{PS}(y,z)\boldsymbol{u}_s(x) = \begin{bmatrix} 1 & 0 & 0 & 0 & -z & y \\ 0 & 1 & 0 & -z & 0 & 0 \\ 0 & 0 & 1 & y & 0 & 0 \end{bmatrix} \begin{bmatrix} u_0 \\ v_0 \\ w_0 \\ \theta_x \\ \theta_y = -w_0' \\ \theta_z = v_0' \end{bmatrix} \tag{6}$$

The resulting strains corresponding to the PS displacement field can be calculated using Eq. (3) and taking into account Eq. (5).

$$\boldsymbol{\varepsilon}^{PS} = \boldsymbol{B}^{PS}(y,z)\boldsymbol{e}_s(x) \tag{7}$$

Where $\mathbf{B}^{PS}(y,z)$ is the strain interpolation matrix according to plain section hypothesis and $\mathbf{e}_s(x) = [\varepsilon_0, \gamma_{0y}, \gamma_{0z}, \phi_y, \phi_z]^T$ is the generalized strain vector of the section or beam defined as usual with ε_0 being the axis elongation, γ_{0y} and γ_{0z} are the generalized shear deformations, ϕ_x as the torsion curvature and finally, ϕ_y and ϕ_z being the bending curvatures. In fact only the elongation and the three curvatures are relevant for the plane section strain calculation so the matrix form of Eq. (7) can be rearranged in a shorter form.

$$\boldsymbol{\varepsilon}^{PS} = \boldsymbol{B}^{*PS}(y,z)\boldsymbol{e}^*_s(x) \tag{8}$$

2.3 Warping distortion displacement field

Differently from classical approaches, this model calculates the warping distortion displacement field in way to consider the complete 3D inter-fiber equilibrium equations explicitly.

$$div\ \boldsymbol{\sigma} = \boldsymbol{L}^T\boldsymbol{\sigma} = \mathbf{0} \tag{9}$$

The previous equation can be rewritten in its weighted residual form:

$$\int_\Omega \delta\boldsymbol{u}^T\boldsymbol{L}^T\boldsymbol{\sigma}d\Omega = \int_L \left(\int_S \delta\boldsymbol{u}^T\boldsymbol{L}^T\boldsymbol{\sigma}dS\right)dL = 0 \tag{10}$$

Where the term between parentheses can be interpreted as the equilibrium residual of a differential portion of the beam.

$$R(x) = \int_S \delta\boldsymbol{u}^T\boldsymbol{L}^T\boldsymbol{\sigma}dS \overset{(i.b.p)}{=} \int_S \delta\boldsymbol{u}^T\boldsymbol{E}_x^T\boldsymbol{\sigma}'dS - \int_S \boldsymbol{L}_{yz}^T\delta\boldsymbol{u}^T\boldsymbol{\sigma}dS = G\left(\boldsymbol{\sigma}'\right) - F\left(\boldsymbol{\sigma}\right) \tag{11}$$

The equilibrium residual, see Eq. (11), can be interpreted as the projection of equilibrium equations on the space of displacements used that means that in order to be in equilibrium in the displacement space, the overall residual along x has to be null.

First the displacement space is reduced to the plane section displacement space, and the residual is computed as follows:

$$R^{PS}(x) = G^{PS}\left(\boldsymbol{\sigma}'\right) - F^{PS}\left(\boldsymbol{\sigma}\right) = \delta\boldsymbol{u}_s^T\int_S \boldsymbol{N}^{PS^T}\boldsymbol{E}_x^T\boldsymbol{\sigma}'dS - \delta\boldsymbol{u}_s^T\int_S \boldsymbol{L}_{yz}\boldsymbol{N}^{PS^T}\boldsymbol{\sigma}dS \tag{12}$$

Making Eq. (12) equals to zero on each cross section of the beam for any $\delta\boldsymbol{u}_s$ constitutes the system of equilibrium equation of the beam element. Also $R^{PS}(x) = 0$ represents the equilibrium among sections of the beam. The integrity of each section meaning the equilibrium among all the fibers in the section is not considered, that's because we reduced the space of possible solution only to $\boldsymbol{u}^{PS}$, so the rest of 3D equilibrium conditions is lost.

Tangential forces (shear forces or torsion moments), produces a stress state that tends to dissociate or delaminate the section's fibers, at this point its possible to differentiate the equilibrium at the beam level ($R^{PS}(x) = 0$) the one among sections of the beam, and the equilibrium at the section level, the one among fibers of the section. See Fig. (4).

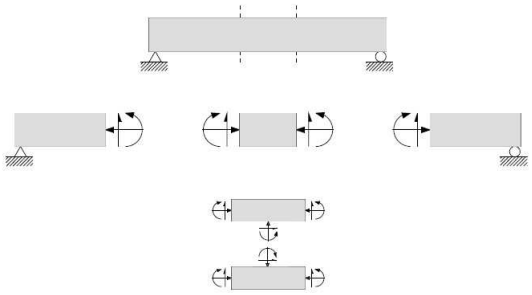

Figure 4: Equilibrium at beam and section level

In order to account for equilibrium among the fibers a more general displacement field space has to be used, but is worth to notice that projecting the equilibrium equations in the whole admissible displacement space is equivalent to the full 3D problem and the benefits of using a beam formulation are lost.

Now in the same way as with the plane section displacement field the residual can be computed in the warping-distortion field.

$$R^W(x) = G^W\left(\boldsymbol{\sigma}'\right) - F^W\left(\boldsymbol{\sigma}\right) = \int_S \delta \boldsymbol{u}_s^{W\,T} \boldsymbol{E}_x^T \boldsymbol{\sigma}' dS - \int_S \boldsymbol{L}_{yz} \delta \boldsymbol{u}_s^{W\,T} \boldsymbol{\sigma} dS \tag{13}$$

The equilibrium conditions can be resumed by the system composed by expressions (12) and (13) where the implicit unknowns are $\boldsymbol{u}^{PS}$ and $\boldsymbol{u}^W$. This system can be rewritten using the stress decomposition presented in Eq. (4).

$$\begin{aligned} R^{PS}(x) = G^{PS}\left(\boldsymbol{\sigma}'\right) - F^{PS}\left(\boldsymbol{\sigma}^{PS}\right) - F^{PS}\left(\boldsymbol{\sigma}^{W}\right) = 0 \\ R^{W}(x) = G^{W}\left(\boldsymbol{\sigma}'\right) - F^{W}\left(\boldsymbol{\sigma}^{PS}\right) - F^{W}\left(\boldsymbol{\sigma}^{W}\right) = 0 \end{aligned} \tag{14}$$

One way to solve this system is to impose $R^W(x) = 0$ at each section of the beam and calculating $\boldsymbol{\sigma}^W$ as a function of $\boldsymbol{u}^{PS}$.

$$\boldsymbol{\sigma}^W = F^{W^{-1}}\left\{G^W\left(\boldsymbol{\sigma}'\right) - F^W\left(\boldsymbol{\sigma}^{PS}\right)\right\} = H^W\left(\boldsymbol{\sigma}', \boldsymbol{\sigma}^{PS}\right) \tag{15}$$

Replacing Eq. (15) on the first equation of system (14) represents the traditional beam equilibrium equations, but considering both components of the stress field.

Expression (15) allows to define a cross section constitutive relation. At beam level equilibrium can be solved using frame elements formulated in the standard fashion. Its remarkable that no fixed shaped of strains or stresses is needed, instead strain patterns are computed from inter-fiber equilibrium in the sectional level.

The warping-distortion displacement field has to be free of body rigid movements, this displacements coincide with the subset of generalized displacements contained in the PS hypothesis $(u_0, v_0, w_0, \theta_x)$. A *priori* both fields, PS and W, can reproduced the previous displacements modes, and uniqueness of solution is not guaranteed. This can be solved forcing $\boldsymbol{u}^W$ to satisfy following equation:

$$\begin{bmatrix} u^R \\ v^R \\ w^R \\ \theta_x^R \end{bmatrix} = \int_S \begin{bmatrix} 1 & 0 & 0 \\ 0 & 1 & 0 \\ 0 & 0 & 1 \\ 0 & -z & y \end{bmatrix} \begin{bmatrix} u^W \\ v^W \\ w^W \end{bmatrix} dS = \begin{bmatrix} 0 \\ 0 \\ 0 \\ 0 \end{bmatrix} \tag{16}$$

This condition is in fact the orthogonality between $\boldsymbol{u}^{PS}$ and $\boldsymbol{u}^{W}$. And also it can be interpreted as imposing the projection of $\boldsymbol{u}^{R}$ on any virtual variation of the rigid displacement to be null.

The warping distortion field is assumed to have the following form:

$$\boldsymbol{u}^{W} = \boldsymbol{U}(y,z)\hat{\boldsymbol{a}} \tag{17}$$

Where $\boldsymbol{U}$ is a matrix of functions in the section space weighted by a coefficient vector $\hat{a}$, defining the distortion of the section. This vector is independent of the x coordinate.

Calculating the residual Eq. (13) on this subspace and using the definition of the plane section strains in expression (8) one obtains:

$$\begin{aligned} R^{W} = & \left[\int_{S} \boldsymbol{U}^{T}\boldsymbol{E}_{x}^{T}\boldsymbol{D}\boldsymbol{B}^{*PS}dS\right]\boldsymbol{e}_{s}^{*\prime} - \left[\int_{S} \boldsymbol{L}_{yz}\left(\boldsymbol{U}\right)^{T}\boldsymbol{D}\boldsymbol{B}^{*PS}dS\right]\boldsymbol{e}_{s}^{*} \\ & - \left[\int_{S} \boldsymbol{L}_{yz}\left(\boldsymbol{U}\right)^{T}\boldsymbol{D}\boldsymbol{L}_{yz}\left(\boldsymbol{U}\right)dS\right]\hat{\boldsymbol{a}} = 0 \\ & = \boldsymbol{A}_{1}\boldsymbol{e}_{s}^{*\prime} - \boldsymbol{B}_{1}\boldsymbol{e}_{s}^{*} - \boldsymbol{C}_{1}\hat{\boldsymbol{a}} = 0 \end{aligned} \tag{18}$$

Where $\boldsymbol{D}$ is the material constitutive matrix. By the previous expression the coefficient vector $\hat{\boldsymbol{a}}$ can be expressed as a function of the generalized strain vector of the section relevant to the plane section hypothesis and its derivatives ξ^{*}.

The distortion displacement field is an implicit function of the generalized strains relevant to the PS hypothesis of the beam. Also $\boldsymbol{u}^{W}$ is determined from information on the same x coordinate and non-local information is obtained through the derivatives of the generalized strains.

$$\boldsymbol{u}^{W} = \boldsymbol{U}(y,z)\hat{\boldsymbol{a}} = \boldsymbol{U}(y,z)\,\boldsymbol{C}_{1}^{-1}\left\{\boldsymbol{A}_{1}\boldsymbol{e}_{s}^{*\prime} - \boldsymbol{B}_{1}\boldsymbol{e}_{s}^{*}\right\} = \boldsymbol{U}(y,z)\boldsymbol{H}_{1}\xi^{*} \tag{19}$$

2.4 Local solution of the warping distortion field

The warping distortion field presented in the previous section is defined through the derivatives of the generalized strains of the section which is a non-local information. In order to make $\boldsymbol{u}^{W}$ only a function of the complete vector of generalized strains $\boldsymbol{e}_{s}$, in other words to express the displacement field only with local information, a relationship between $\boldsymbol{e}_{s}^{*}$ and $\boldsymbol{e}_{s}^{*\prime}$ is needed. This can be done thanks to an additional equilibrium condition and to the fact that the components of $\boldsymbol{e}_{s}^{*\prime}$ are not independent.

First of all ${\varepsilon_{0}}'$ and ${\phi_{x}}'$ can be calculated from the conditions that ${N_{x}}' = 0$ and ${M_{x}}' = 0$, because they can be condensed in the cross section domain. Also both derivatives of curvature are related to the corresponding generalized shear deformations γ_{0y} and γ_{0z}. Taking this into account one may write the following relationships.

$$\boldsymbol{u}^{W} = \boldsymbol{A}\left(\boldsymbol{e}_{s}\right) \tag{20}$$

$$\boldsymbol{\varepsilon}^{W} = \boldsymbol{L}\boldsymbol{A}\left(\boldsymbol{e}_{s}\right) = \boldsymbol{B}^{W}\boldsymbol{e}_{s} \tag{21}$$

$$\boldsymbol{\sigma}^{PS} = \int \boldsymbol{D}d\boldsymbol{\varepsilon}^{PS}\ ;\ \boldsymbol{\sigma}^{W} = \int \boldsymbol{D}d\boldsymbol{\varepsilon}^{W} \tag{22}$$

2.5 Generalized stresses. Section's stiffness matrix

The calculation of generalized stresses is made through the Virtual Work Principle as follows:

$$\int_L \delta \boldsymbol{e}_s^T \boldsymbol{s}_s dL = \int_L \left(\int_S \delta \boldsymbol{\varepsilon}_s^T \boldsymbol{\sigma} dS \right) dL$$
$$\Rightarrow \delta \boldsymbol{e}_s^T \boldsymbol{s}_s = \int_S \delta \boldsymbol{\varepsilon}_s^T \boldsymbol{\sigma} dS = \delta \boldsymbol{e}_s^T \left[\int_S \boldsymbol{B}^{PS^T} \boldsymbol{\sigma} dS + \int_S \boldsymbol{B}^{W^T} \boldsymbol{\sigma} dS \right] \tag{23}$$

$$\boldsymbol{s}_s = \int_S \boldsymbol{B}^{PS^T} \boldsymbol{\sigma} dS + \int_S \boldsymbol{B}^{W^T} \boldsymbol{\sigma} dS = \boldsymbol{s}_s^{PS} + \boldsymbol{s}_s^W \tag{24}$$

To calculate the sections stiffness matrix of the cross section, linearization of expression (24) has to be made:

$$\dot{\boldsymbol{s}}_s = \int_S \boldsymbol{B}^{PS^T} \boldsymbol{D} \dot{\boldsymbol{\varepsilon}} dS + \int_S \boldsymbol{B}^{W^T} \boldsymbol{D} \dot{\boldsymbol{\varepsilon}} dS \tag{25}$$

After decomposition of strains and using expression (21) and (7) the section's stiffness matrix results:

$$\boldsymbol{K}_s = \int_s \left[\boldsymbol{B}^{PS^T} \boldsymbol{D} \boldsymbol{B}^{PS} + \boldsymbol{B}^{PS^T} \boldsymbol{D} \boldsymbol{B}^{W} + \boldsymbol{B}^{W^T} \boldsymbol{D} \boldsymbol{B}^{PS} + \boldsymbol{B}^{W^T} \boldsymbol{D} \boldsymbol{B}^{W} \right] dS \tag{26}$$

2.6 Numerical implementation

The model presented in the previous sections is implemented in a finite element environment for sectional analysis where the cross section is discretized into bidimensional elements (quadrangular or triangular elements can be used) with first order Lagrange polynomials as interpolation function and Gauss-Legendre quadrature as integration rule that represent the solid matrix of the section. Also 2 node linear Lagrange elements representing transverse reinforcements is used. Finally a point element representing longitudinal reinforcement intersecting the cross section is used. This three elements are the minimum required to model a typical reinforced concrete section. See Fig. (5).

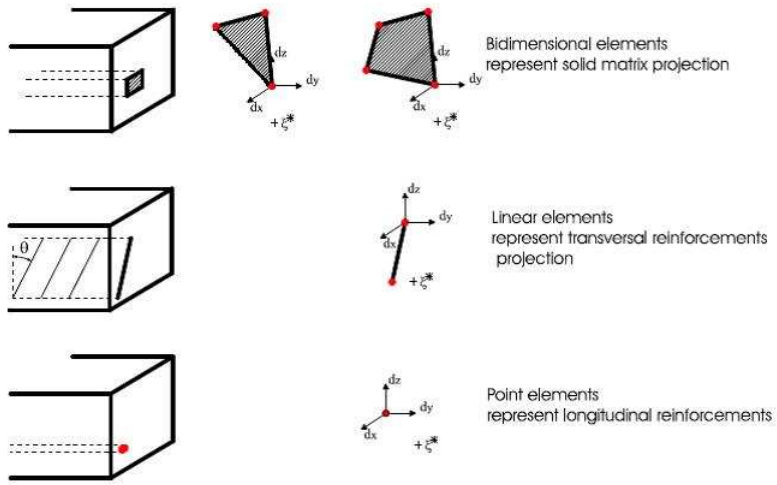

Figure 5: Elements for sectional discretization

3 PLASTIC-DAMAGE MODEL FOR CONCRETE

Four material constitutive models where originally implemented in the FE code. Three of them are 3D constitutive models to represent material behavior of the solid matrix of the cross section, an additional uniaxial constitutive law is implemented to represent material behavior of either transverse or longitudinal reinforcements. In order to contribute to the improvement of the finite element code and to extend his capabilities, a continuous concrete constitutive model is presented and implemented.

The constitutive model implemented in the finite element code is the one presented by Lee and Fenves (1998) that is in fact an extension to the cyclic loading case of the Barcelona Model presented by Lubliner et al. (1989). This is a plastic-damage model based in the plasticity theory that introduces two damage internal variables using the concept of fracture-energy damage, also it introduces two stiffness degradation scalar variables based in isotropic continuum damage mechanics and in the effective stress concept. The model uses a new yield surface as a criterion and a different plastic potential surface in order to match experimental data, this leads to a non-associative flow rule that causes a non-symmetric tangent stiffness matrix.

3.1 Main features

The main aspects of the model are summarized in the following. First of all, as usual in plasticity theories, the strain is decomposed into the elastic and plastic parts.

$$\begin{aligned} \boldsymbol{\varepsilon} &= \boldsymbol{\varepsilon}^e + \boldsymbol{\varepsilon}^p \\ \boldsymbol{\varepsilon}^e &= \boldsymbol{E}^{-1}\boldsymbol{\sigma} \\ \boldsymbol{\sigma} &= \boldsymbol{E} : (\boldsymbol{\varepsilon} - \boldsymbol{\varepsilon}^p) \end{aligned} \tag{27}$$

Where $\boldsymbol{E}$ is the elastic stiffness four rank tensor. Also, introducing the concept of effective stresses from continuum damage mechanics, it can be seen that stresses can be mapped into effective stress through a four rank tensor $\boldsymbol{D}$, but the hypothesis of isotropic degradation is made so this can be simplified as follows:

$$\begin{aligned} \bar{\boldsymbol{\sigma}} = \boldsymbol{D} : \boldsymbol{\sigma} = \frac{1}{(1-D)}\boldsymbol{I} : \boldsymbol{\sigma} = \frac{1}{(1-D)}\boldsymbol{\sigma} = \boldsymbol{E}_0 : (\boldsymbol{\varepsilon} - \boldsymbol{\varepsilon}^p) \\ \boldsymbol{E} = (1-D)\boldsymbol{E}_0 \end{aligned} \tag{28}$$

In (28) the scalar degradation of the elastic stiffness variable D has a value between zero, where no degradation had place, and one where full degradation is assumed $(0 \leq D < 1)$. Also in the previous expression $\boldsymbol{E}_0$ is the initial elastic stiffness tensor.

Another important aspect of any plasticity model is the evolution of the plastic strains. This is made as usual by means of the normality rule, so a plastic potential function is needed. Is worth to mentioned that to improve the numerical implementation, the elastoplastic response is separated, by means of the effective stress concept, of the degradation process so this plastic potential function has to be defined in the effective stress space.

$$\dot{\boldsymbol{\varepsilon}^p} = \dot{\lambda}\frac{\partial \phi}{\partial \bar{\boldsymbol{\sigma}}}(\bar{\boldsymbol{\sigma}}) \tag{29}$$

Where λ is the plastic consistency parameter, and ϕ is the plastic potential function.

In order to take into account the different damage states another internal variable is introduced, $\boldsymbol{\kappa}$. The components of this 2D vector variable are the damage in tension and in compres-

sion parameters $\boldsymbol{\kappa}\,(\kappa_t, \kappa_c)$, the evolution of this variable is given by:

$$\dot{\boldsymbol{\kappa}} = \dot{\lambda}\boldsymbol{H}\,(\bar{\boldsymbol{\sigma}}, \boldsymbol{\kappa}) \tag{30}$$

A yield criterion is needed to complete the elastoplastic model. This yield surface is able to evolve during the damage process so it will be seen that the damage variable plays the role of the hardening variable in classic plasticity models. Here hardening has to be understand in a broad sense including softening as well as hardening processes. Eq. (31).

$$\widetilde{F} = (\boldsymbol{\sigma}, f_t, f_c) \leq 0 \tag{31}$$

Where (f_t, f_c), the uniaxial strength functions, are explicit functions of (κ_t, κ_c) and they control the evolution of the yield surface. Introducing the stiffness degradation variable D, see Eq. (28) which is also an explicit function of $\boldsymbol{\kappa}$, the yield surface Eq. (31) can now be rewritten in the effective stress space and also as function of the damage variable, which plays the role of hardening variable.

$$F\,(\bar{\boldsymbol{\sigma}}, \boldsymbol{\kappa}) \leq 0 \tag{32}$$

The elastoplastic response of the plastic-damage model is described in terms of the effective stresses, the plastic strains and the damage variable by equations (28), (29), (30) and (32). Additionally loading/unloading conditions are needed to represent the cyclic behavior. These are the Kuhn-Tucker optimization conditions and the consistency condition.

$$\begin{aligned} \dot{\lambda} &\geq 0 \\ \dot{\lambda}F &= 0 \\ F &\leq 0 \end{aligned} \tag{33}$$

Finally the total stresses are computed after evaluating the degradation variable D,

$$\boldsymbol{\sigma} = [1 - D\,(\boldsymbol{\kappa})]\,\bar{\boldsymbol{\sigma}} \tag{34}$$

3.2 Damage variable - Evolution of internal variables

The damage variable in cohesive-frictional materials can be defined as a relative measure of the energy dissipated during an inelastic process.

For simplicity the damage variable is presented in the for a uniaxial process $\aleph$, either in compression or tension $\aleph \in (t, c)$. Assuming that from the stress-strains diagrams obtained through uniaxial tests the stress-plastic strains diagrams can be constructed, see Fig.6, and that the area under these curves is assumed to be finite, the damage variable can be defined as follows:

$$\kappa_\aleph = \frac{1}{g_\aleph}\int_0^{\varepsilon^p} \sigma_\aleph\,(\varepsilon^p)\,d\varepsilon^p \tag{35}$$

$$g_\aleph = \int_0^{\infty} \sigma_\aleph\,(\varepsilon^p)\,d\varepsilon^p \tag{36}$$

The quantities (g_t, g_c), in expression (36), cannot be only material properties. It is well known that frictional solids tend to concentrate the dissipation of energy in an infinitesimal

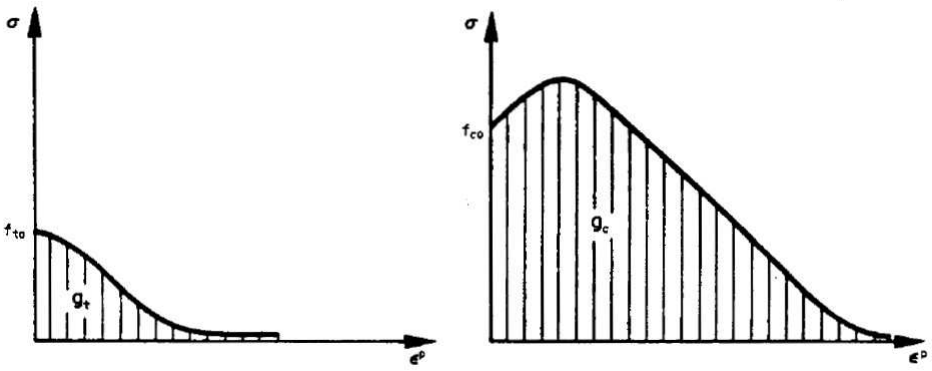

Figure 6: Uniaxial curves (σ, ε^p) in tension and compression

volume. In order to treat this phenomena by means of a continuous solid mechanic theory, it is necessary to introduce a characteristic length that will depend on the FE mesh size. The definition of this length was explained in detail by Oliver (1989) and by Bazant (1976, 1983). So both are now defined as:

$$g_{\aleph} = \frac{G_{\aleph}}{l_{ch}} \tag{37}$$

Where l_{ch} is the characteristic length of the mesh and $G_{\aleph}$ is assumed to be a material property. In the tension case can be interpreted as the specific fracture energy defined as the energy required to form a unit area of crack. And in the compression case, only the post peak part of the curve is mesh-sensitive so it can be decomposed in two parts, one mesh-independent and other mesh-dependent.

Taking into account (35) the damage variable in a uniaxial process can be written:

$$\dot{\kappa_{\aleph}} = \frac{1}{g_{\aleph}} f_{\aleph}\left(\kappa_{\aleph}\right) \dot{\varepsilon^p} \tag{38}$$

To extend the uniaxial version of the evolution of damage to the multiaxial case, the scalar plastic strain rate in the general case can be calculated as follows:

$$\dot{\varepsilon^p} = \delta_{t\aleph}\, r\left(\hat{\boldsymbol{\sigma}}\right) \hat{\dot{\varepsilon}}^{\,p}_{max} + \delta_{c\aleph}\left[1 - r\left(\hat{\boldsymbol{\sigma}}\right)\right] \hat{\dot{\varepsilon}}^{\,p}_{min} \tag{39}$$

Where δ is the Kronecker's delta, $\hat{\dot{\varepsilon}}^{\,p}_{max}$ and $\hat{\dot{\varepsilon}}^{\,p}_{max}$ are the minimum and maximum eigenvalues of the plastic strain tensor. The weight factor $r\left(\hat{\boldsymbol{\sigma}}\right)$ depends on the eigenvalues of the effective stress tensor and its equal to zero for triaxial compression and equals to one for triaxial tension.

Evolution laws in expressions (29) and (30) can be modified into relations in the principal space of effective stresses and strains.

$$\begin{aligned} \hat{\dot{\boldsymbol{\varepsilon}}}^{\,p} &= \dot{\lambda} \frac{\partial \phi}{\partial \hat{\boldsymbol{\sigma}}}\left(\hat{\boldsymbol{\sigma}}\right) \\ \dot{\boldsymbol{\kappa}} &= \dot{\lambda} \hat{\boldsymbol{H}}\left(\hat{\boldsymbol{\sigma}}, \boldsymbol{\kappa}\right) \end{aligned} \tag{40}$$

3.3 Yield surface and plastic potential function

The yield surface used in this model was first introduced by Lubliner et al. (1989) as an improvement of classical yield functions for frictional materials as the Mohr-Coulomb or Drucker-

Prager criteria. Fig.7

$$F(\boldsymbol{\sigma}, \boldsymbol{\kappa}) = \frac{1}{1-\alpha}\left[\alpha I_1 + \sqrt{3J_2} + \beta(\boldsymbol{\kappa})\langle\hat{\sigma}_{max}\rangle\right] - c_c(\boldsymbol{\kappa}) \leq 0 \tag{41}$$

Where $I_1 = tr(\boldsymbol{\sigma})$, $J_2 = \frac{1}{2}\boldsymbol{s} : \boldsymbol{s}$, α and β are dimensionless parameters and $\hat{\sigma}_{max}$ is the largest eigenvalue of the stress tensor.

The α parameter in (41) is computed in order to match experimental data specially to control the enhancement in the yield stress that concrete exhibits in biaxial compression, so α is determined by comparing the uniaxial with the biaxial yield stress.

The parameter was firstly introduced as a constant by Lubliner et al. (1989) for monotonic loading cases, and then it was defined as function of the damage variable by Lee and Fenves (1998) in order to extend the model to the cyclic loading case. This parameter allows the model to adjust the relationship between the uniaxial strength in compression and in tension.

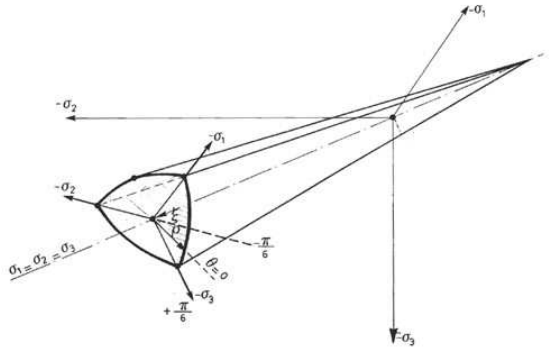

Figure 7: Yield surface in the Westergaard space

Is worth to notice that the yield surface presented is open in the direction of hydrostatic compression. This is equivalent to assume that no yielding is reached for hydrostatic compression. It can be seen that the yield surface has a conic shape in the effective stress space, in the π plane also it describes a three vertex curve, and also has a vertex in the uniaxial compression point and in the biaxial tension point. All this singularities produce a multiple definition of the normal vector of the yield surface which is needed for the definition of the tangent stiffness tensor.

The plastic flow rule in expression (40) states that the plastic flow direction is defined by the normal vector of the plastic potential surface. Lee and Fenves (1998) proposed the linear version of the Drucker-Prager criteria, but is well known that this surface has a singularity at the triaxial tension point, so Omidi and Lofti (2010) used a hyperbolic version of Drucker-Prager surface in order to avoid this singularity.

$$\phi(\bar{\boldsymbol{\sigma}}) = \sqrt{(\varepsilon_1 \alpha_p f_{t0})^2 + 2J_2} + \alpha_p I_1 \tag{42}$$

Where ε_1 is a constant that adjusts the eccentricity of the hyperbolic function from the apex in the linear function. The α_p parameter controls the dilatancy of the model and is held constant during the whole analysis. The choice of a non-associative plasticity is made in order to fit properly experimental results, using two different functions one for the yield surface and one for the plastic potential function will cause the non-symmetry of the stiffness tensor. Finally the plastic potential function presented in (42) is a continuous and smooth function where the flow direction is always uniquely defined.

3.4 Stiffness degradation

The stiffness degradation caused by the microcracking either in tension or compression is treated separately from the elastoplastic response. In the cyclic loading case the phenomenon of crack opening and closing during unloading or reloading process has to be represented by the model. See Fig.(8).

$$\begin{gathered} D = D\left(\bar{\boldsymbol{\sigma}}, \boldsymbol{\kappa}\right) = 1 - \left[1 - s_t\left(\bar{\boldsymbol{\sigma}}\right) D_t\left(\kappa_t\right)\right]\left[1 - s_c\left(\bar{\boldsymbol{\sigma}}\right) D_c\left(\kappa_c\right)\right] \\ 0 \leq \left(s_t, s_c\right) \leq 1 \\ s_t\left(\bar{\boldsymbol{\sigma}}\right) = 1 - w_t\, r\left(\hat{\bar{\boldsymbol{\sigma}}}\right) \\ s_c\left(\bar{\boldsymbol{\sigma}}\right) = 1 - w_c\left(1 - r\left(\hat{\bar{\boldsymbol{\sigma}}}\right)\right) \end{gathered} \tag{43}$$

Where w_t and w_c are the stiffness recovery factors that will be chosen in order to match the experimental data. In the case of concrete this factors are $w_t = 0$ and $w_c = 1$.

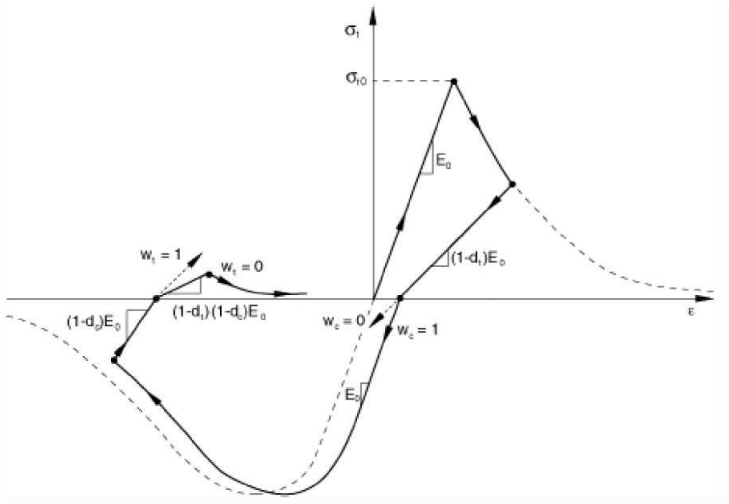

Figure 8: Stiffness recovery factors

3.5 Integration and numerical implementation - Stiffness matrix

The numerical integration of the plastic-damage model is made through time discretization of the evolution equations and the backward-Euler method is used, this method is unconditionally stable and has first order precision. It can be seen also has the generalized trapeze method with the α parameter equal to one.

The numerical algorithm in Fig.(9) is a strain-driven discrete problem. Each new step will have has an input the last converged step values of the problem variables $\{\boldsymbol{\varepsilon}_{\boldsymbol{n}}^{\boldsymbol{p}}, \boldsymbol{\kappa}_{\boldsymbol{n}}, D_n\}$. The last input of the algorithm is the strain tensor of the new step $\boldsymbol{\varepsilon}_{\boldsymbol{n+1}}$.

The stress computation can be arranged in a three step calculation method. First an elastic predictor is made by means of the trial effective tensor, the second step is a plastic corrector step and finally in an uncoupled way a damage corrector is introduced. In order to solve the stress computation in a more efficient way a spectral returning algorithm based on the spectral decomposition of the effective stresses is used. This is done because of the form of this yield function, it can be seen in (41) that the function includes principal stress terms in addition of the tensor invariants so in this cases is more efficient to work with the eigenvalues matrix.

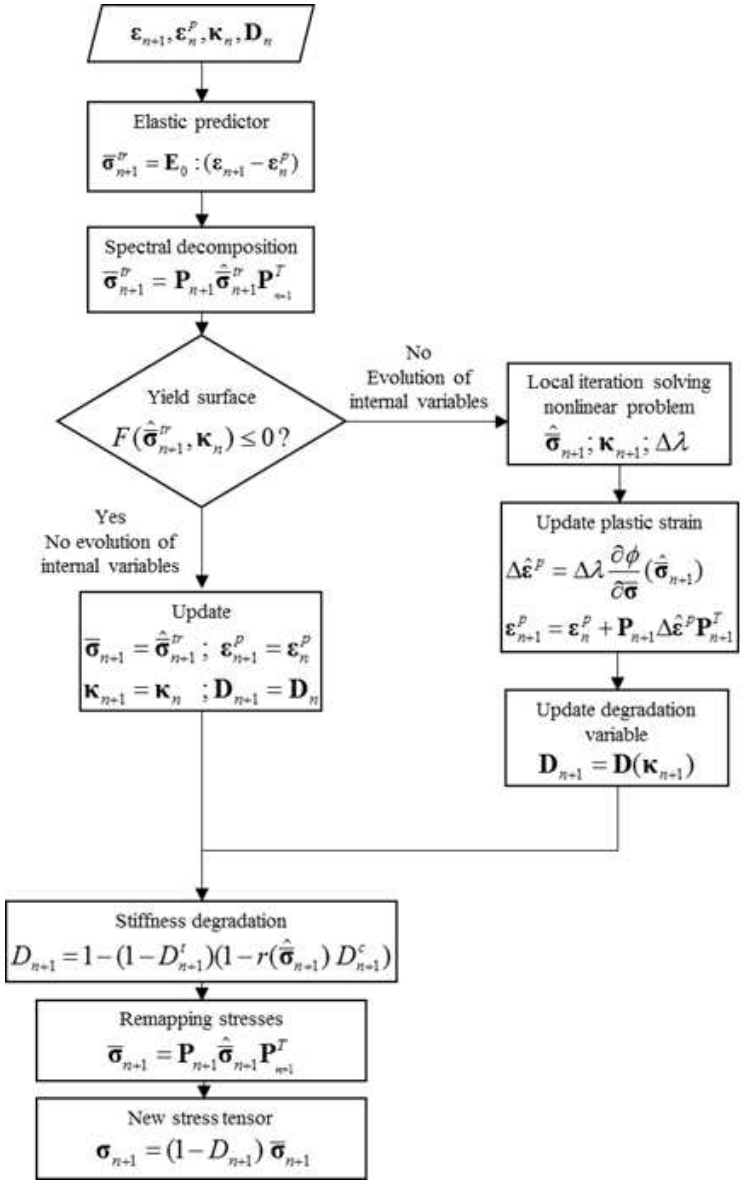

Figure 9: Constitutive model flow chart

Both evolution equations of the internal variables (40) are solved by means of the backward-Euler method, and the nonlinear problem in the evolution of the damage variable is solved by a Newton-Raphson solver.

Finally, in nonlinear problems the rate of convergence of the nonlinear solver depends strongly on the tangent stiffness matrix that's being used. Lee and Fenves (1998) presented the continuum tangent stiffness of the model, and later Lee and Fenves (2001) presented an algorithmic tangent stiffness consistent with the stress updating algorithm described in the previous section. Both matrices were analyzed but in this work a numerical stiffness matrix was implemented because of the simplicity in the implementation.

The numerical stiffness matrix is calculated once the updating stress algorithm reached the new converged state. Each column of the stiffness matrix is calculated introducing a perturbation on the corresponding term of the strain tensor.

$$\widetilde{\varepsilon}_{n+1}^q = \{\varepsilon_{n+1}^1, \cdots, \varepsilon_{n+1}^q + h, \cdots, \varepsilon_{n+1}^6\}^T \tag{44}$$

Where h is a numerical perturbation that is determined as multiple of the machine precision. With this new strain tensor, and using the updating stress algorithm a new perturbed stress is calculated

$$\left[\widetilde{\boldsymbol{\varepsilon}}^{q}_{n+1}; \boldsymbol{\varepsilon_{n+1}}; \boldsymbol{\kappa_{n+1}}; D_{n+1}\right] \rightarrow Updating\ stress\ algorithm \rightarrow \widetilde{\boldsymbol{\sigma}}^{q}_{n+1} \tag{45}$$

Finally the q-column of the tangent matrix is calculated as:

$$\boldsymbol{E}^{q} = \frac{1}{h}\left(\widetilde{\boldsymbol{\sigma}}^{q}_{n+1} - \boldsymbol{\sigma}_{n+1}\right) \tag{46}$$

This procedure is repeated for each component of the strain tensor and the stiffness matrix is finally the concatenation of the six columns calculated with expression (46).

4 UNIFIED LIBRARY OF NONLINEAR SOLVERS

The TINSA code for sectional analysis has two different ways to solve the nonlinear problem. A Newton-Raphson method as load control method and a displacement control method are implemented as well as a substepping strategy in order to improve the convergence of the solver.

In order to improve the ability to treat highly nonlinear problems a new library of nonlinear solvers presented by Leon et al. (2011) is implemented in the TINSA code. This library consists in a unified framework that allows to introduce different nonlinear solution schemes with the same algorithm.

The unified framework is presented in the following. Four methods are implemented using this framework the load control method (Newton-Raphson), the displacement control method, the arc-length control method and the work control method. Is worth to mention that even only this four methods were implemented the unified scheme allows the implementation of other control methods.

4.1 Unified nonlinear framework

The unified nonlinear formulation is a usual incremental-iterative procedure where the load is applied in incremental steps and iterations are performed at each incremental step until the convergence criterion is satisfied. See Fig.(10).

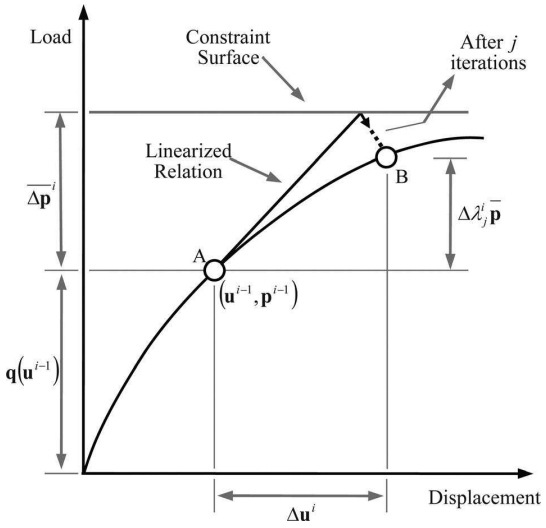

Figure 10: Incremental-iterative procedure

In structural nonlinear analysis the unbalanced force vector to be minimized in i-incremental step and in the j-iteration can be written as follows:

$$\boldsymbol{r}_j^i = \boldsymbol{p}_j^i - \boldsymbol{q}\left(\boldsymbol{u}_j^i\right) \tag{47}$$

Where $\boldsymbol{p}_j^i$, is the vector of applied external forces and $\boldsymbol{q}_j^i$ is the vector of internal forces which is a function of the displacements $\boldsymbol{u}_j^i$. In the incremental-iterative procedure the loads and displacements are computed by adding to the previous converged step the incremental updates at the current j–iteration.

$$\begin{aligned} \boldsymbol{u}_j^i &= \boldsymbol{u}^{i-1} + \Delta\boldsymbol{u}_j^i \\ \boldsymbol{p}_j^i &= \boldsymbol{p}^{i-1} + \Delta\boldsymbol{p}_j^i \end{aligned} \tag{48}$$

On each iteration the incremental updates presented in (48) are calculated in a similar way by adding the contribution of the previous iteration and the iterative updates at the current iteration.

$$\begin{aligned} \Delta\boldsymbol{u}_j^i &= \Delta\boldsymbol{u}_{j-1}^i + \delta\boldsymbol{u}_j^i \\ \Delta\boldsymbol{p}_j^i &= \Delta\boldsymbol{p}_{j-1}^i + \delta\boldsymbol{p}_j^i \end{aligned} \tag{49}$$

Taking (48) into account int the residual vector (47) can be rewritten as:

$$\boldsymbol{r}_j^i = \boldsymbol{p}^{i-1} + \Delta\boldsymbol{p}_j^i - \boldsymbol{q}\left(\boldsymbol{u}^{i-1} + \Delta\boldsymbol{u}_j^i\right) \tag{50}$$

Finally the equation to be solved at the j–iteration of i–increment that governs the response of the structure is:

$$\boldsymbol{K}_{j-1}^i \delta\boldsymbol{u}_j^i = \boldsymbol{p}_j^i - \boldsymbol{q}_{j-1}^i \tag{51}$$

Where $\boldsymbol{K}_{j-1}^i$, is the tangent matrix of the structure.

Introducing into equations (48) and (49) the load factor parameter λ and the reference load vector $\bar{\boldsymbol{p}}$, the iterative form of the external applied load vector and the governing equation of the system can be rewritten as follows:

$$\begin{aligned} \boldsymbol{p}_j^i &= \boldsymbol{p}^{i-1} + \Delta\boldsymbol{p}_{j-1}^i + \delta\lambda_j^i\bar{\boldsymbol{p}} \\ \boldsymbol{K}_{j-1}^i \delta\boldsymbol{u}_j^i &= \boldsymbol{r}_{j-1}^i + \delta\lambda_j^i\bar{\boldsymbol{p}} \end{aligned} \tag{52}$$

Equation (52) is a set of N equations, being N the degrees of freedom of the system, with $N+1$ unknowns: the N displacements $\delta\boldsymbol{u}_j^i$ and the load parameter $\delta\lambda_j^i$. In order to solve the system an additional constrain equation must be added.

$$\boldsymbol{a}_j^i \cdot \delta\boldsymbol{u}_j^i + b_j^i \delta\lambda_j^i = c_j^i \tag{53}$$

The system of $N+1$ unknowns and $N+1$ equations formed by (52) and (53) can be summarized in a matrix form as follows:

$$\begin{bmatrix} \boldsymbol{K}_{j-1}^i & -\bar{\boldsymbol{p}} \\ \left(\boldsymbol{a}_j^i\right)^T & b_j^i \end{bmatrix} \begin{Bmatrix} \delta\boldsymbol{u}_j^i \\ \delta\lambda_j^i \end{Bmatrix} = \begin{Bmatrix} \boldsymbol{r}_{j-1}^i \\ c_j^i \end{Bmatrix} \tag{54}$$

The new system's matrix presented in (54) is no longer symmetric and also the bandwidth has been modified from the original tangent stiffness matrix. This may cause a low computational

efficiency when solving the system by means of traditional linear solvers. To overcome this problem the decomposition of the displacement iteration update is introduced.

$$\begin{aligned} \delta \boldsymbol{u}_j^i &= \delta\lambda_j^i \delta \boldsymbol{u}_{p_j}{}^i + \delta \boldsymbol{u}_{r_j}{}^i \\ \boldsymbol{K}_{j-1}^i \delta \boldsymbol{u}_{p_j}{}^i &= \bar{\boldsymbol{p}} \\ \boldsymbol{K}_{j-1}^i \delta \boldsymbol{u}_{r_j}{}^i &= \boldsymbol{r}_{j-1}^i \end{aligned} \tag{55}$$

Finally the load parameter which is needed to compute the total displacement for the j–iteration at i–increment, can be calculated using the constraint equation (53) and the displacement decomposition (55) as follows:

$$\delta\lambda_j^i = \frac{c_j^i - \boldsymbol{a}_j^i \cdot \delta \boldsymbol{u}_{r_j}{}^i}{\boldsymbol{a}_j^i \cdot \delta \boldsymbol{u}_{p_j}{}^i + b_j^i} \tag{56}$$

The benefit of using this unified framework is the fact that each nonlinear solution scheme differs only in the constraint equation and they can be solved by the same algorithm where only the calculation of the parameters of equation (53) and consequently the calculation of the load factor are different for each scheme.

The algorithm is implemented in the TINSA code following the flow chart in Fig.(11), additionally for each nonlinear solution scheme a function to calculate the load factor parameter is implemented. Is remarkable that the code allows the simple implementation of other nonlinear solutions by means of this "function" structure.

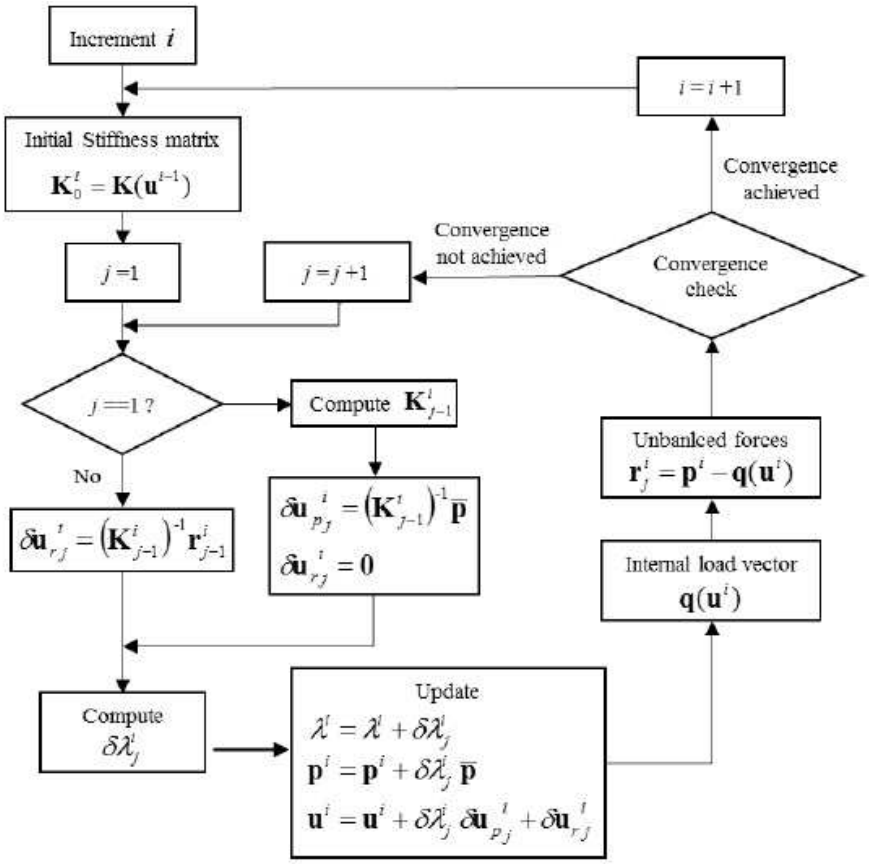

Figure 11: Unified scheme flow chart

Four different control methods are implemented under the form of the unified framework previously presented. The load control method or Newton-Raphson methods where the external loads are computed at the first iteration of each increment and held constant in the remaining iterations. The displacement control method which uses a fixed displacement component as the control parameter to trace the structural response. The arc-length control method that considers simultaneous iterations on the load and displacements variables, the method is based in the constraint of the solution to an arc-length. And finally the work control method which uses a constant work increment thought the iterations of an increment, this method was introduced to overcome to the unit problem in the arc-length method.

Each nonlinear scheme has its own advantages and weakness so the user may choose between the different schemes depending on the nonlinear problem to solve. For example the load control method fails to reproduce load limits points and softening parts, while the displacement can capture load limit points and softening responses but it fails to near displacements limits points. The arc-length method is able to reproduce complex nonlinear problems with load and displacement limit points or snap-back phenomena but it has units problems because it uses the displacement vector where the displacement and rotation components has different orders of magnitude, which may cause incorrect changes in the sense of the response.

5 APPLICATION EXAMPLES

In order to show the capabilities of the TINSA code with the new plastic-damage model and the new library of nonlinear solvers three analysis of reinforced concrete sections are presented in this chapter. The first case shows the influence of the concomitant shear force in the moment-curvature curve of a rectangular reinforced concrete section. Finally the experimental results of a prestressed concrete beam are compared with the numerical prediction of TINSA.

5.1 Moment-curvature of a reinforced concrete section with shear forces

Traditionally in the nonlinear analysis of reinforced concrete frames the nonlinear response of the frame elements is characterized by the moment-curvature $(M-\phi)$ curve, so several beam models uses this curve as an input. Also this curve allows the simply identification of characteristic points and properties of the section as the cracking and yielding points and the ductility of the section.

Is well known that the concomitance of axial forces has an important influence on the $(M-\phi)$ curve, a moderate axial compression reduces the sections ductility and increases the resisting moment. This phenomenon can be captured by traditional fiber beams element based in the NB kinematic hypothesis. In the other hand the influence of a concomitant shear force is not clear and models that neglect the inter-fiber equilibrium are not capable of reproducing this phenomenon.

The $(M-\phi)$ curves of a rectangular reinforced concrete section are obtained with TINSA using the plastic-damage model and the displacement control method for different levels of shear force which is quantified as the shear span to effective depth ratio (M/Vd).

The geometry, reinforcement and discretization of the concrete section can be seen in Fig.(12). Also material properties of concrete, the longitudinal and transverse steel reinforcement are summarized in Table (1) and Table (2).

The obtained curves for shear span ratios of 2, 3, 4 and 5 are presented in Fig.(13). Also the deformed shape of the section showing the warping of the cross-section and the distribution of the tension damage variable for the shear span ratio of 5 are presented in Fig.(14).

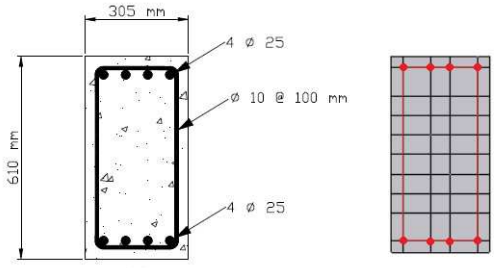

Figure 12: Cross-section - Geometry discretization

$E_0 =$	$25600N/mm^2$		$G_t =$	$0.133N/mm$
$\nu =$	0.2		$G_c =$	$13.3N/mm$
$f'_c =$	$28.2N/mm^2$		$\widetilde{D}_t =$	0.51
$f_{0c} =$	$16.9N/mm^2$		$\widetilde{D}_c =$	0.38
$f_t =$	$1.75N/mm^2$		$\alpha_p =$	0.25
$\frac{f_{0b}}{f_{0c}} =$	1.16	ε_1=0.1	$l_{ch} =$	$35mm$

Table 1: Concrete properties

Longitudinal Reinforcement	$E_s =$	$200000MPa$
	$E_p =$	$200MPa$
	$f_y =$	$442MPa$
Transverse Reinforcement	$E_s =$	$200000MPa$
	$E_p =$	$200MPa$
	$f_y =$	$400MPa$

Table 2: Reinforcement properties

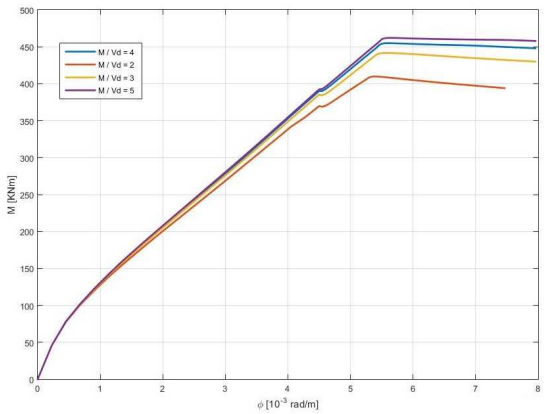

Figure 13: Moment-curvature for different shear levels

It can be seen that the shear has an influence in several nonlinear characteristics of the section, the yielding moment is clearly affected by the concomitant shear force, also both post-cracking and post-yielding stiffness are reduced when shear forces increases. Fig.(15) shows the distribution of normal stresses at the same curvature level for the shear-span ratio of 5 and 2, it can be seen that the axial stress is almost null in the cracked zone for the shear-span ratio of 5 and in the case of the shear-span ratio of 2 where the shear influence is higher the cracked zone presents

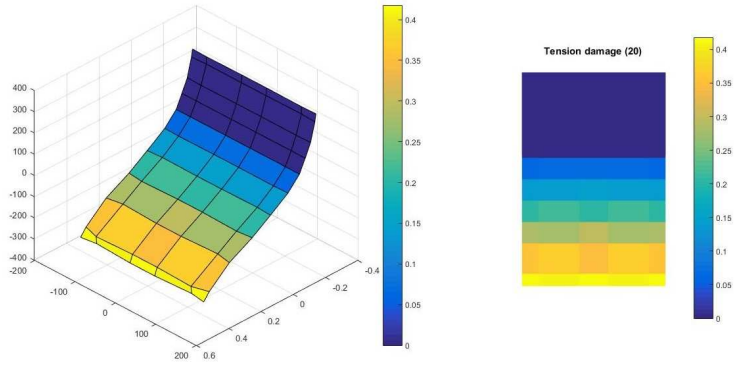

Figure 14: Warping - Distribution of κ_t for $M/Vd = 5$

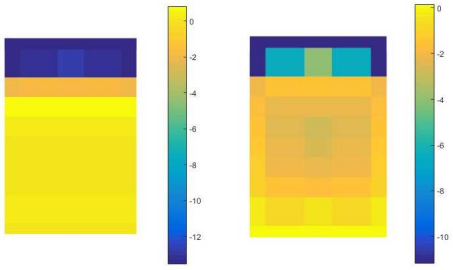

Figure 15: σ_{xx} distribution at $\phi = 6x10^{-3}$ for $M/Vd = 5$ and $M/Vd = 2$

compression in the cracked zone this is because the concomitant shear effort that produces this stresses. Finally it can be seen in the shear-span ration of 2 a reduction of ductility.

5.2 Sectional analysis of a prestressed concrete beam

One section belonging to the first of eight beams of an experimental campaign of prestressed reinforced concrete beams carried out at the *Laboratori de Tecnologia d'Estructures - Universitat Politècnica de Catalunya*, is analyzed using TINSA with the plastic-damage model, and numerical prediction is compared with experimental results. In the following the test characteristics and numerical model are presented.

The test consist on a simply supported prestessed reinforced concrete beam of double T cross-section with a point load applied by a hydraulic jack. See Fig.(16).

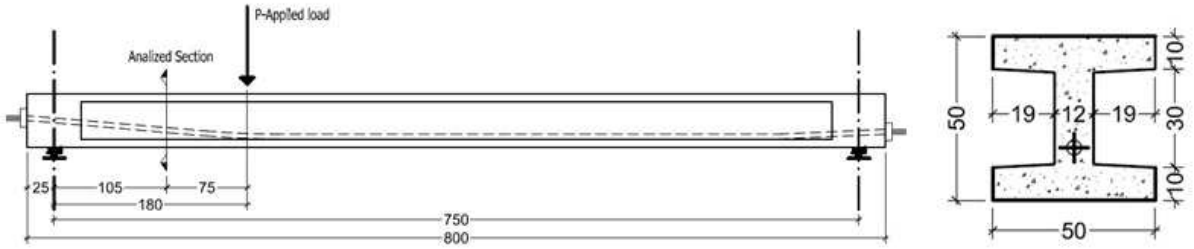

Figure 16: General geometry of the test (dimensions in cm)

The analyzed section corresponds to the one with highest shear effort. Fig.(17) shows the detailing of reinforcement which is composed of active and passive steel for the longitudinal

reinforcements and passive steel is used for the transversal reinforcement.

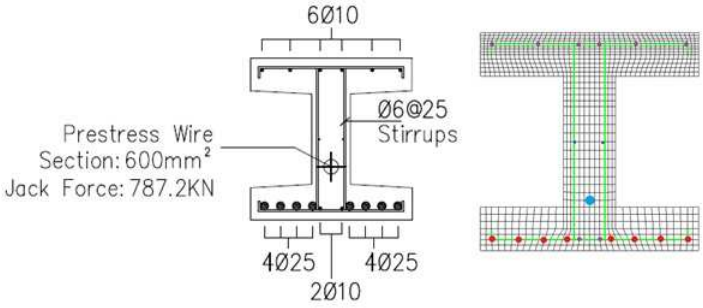

Figure 17: Reinforcement detail of the analyzed cross section - FE mesh

The numerical model uses the finite element mesh presented in Fig.(17) where the concrete solid matrix is meshed using quadrangular elements, the transverse reinforcement is modeled with linear elements and longitudinal reinforcement both passive and active are represented by point elements. In order to introduce the prestress force, in the point element that corresponds to the prestress wire an initial pre-strain is introduce and by means of material properties the corresponding force is applied.

The material properties were obtained by compression and Brazilian-tension tests of cylindrical specimens casted at the same time as the beam. Also tension tests of the reinforcement bars were carried out in order to obtain the steel properties. Table(3) and table (4) summarizes the material properties used in the numerical model.

$E_0 =$	$28000N/mm^2$		$G_t =$	$0.142N/mm$
$\nu =$	0.2		$G_c =$	$14.2N/mm$
$f'_c =$	$40N/mm^2$		$\widetilde{D}_t =$	0.51
$f_{0c} =$	$24N/mm^2$		$\widetilde{D}_c =$	0.38
$f_t =$	$3.18N/mm^2$		$\alpha_p =$	0.25
$\frac{f_{0b}}{f_{0c}} =$	1.16	ε_1=0.1	$l_{ch} =$	$11.3mm$

Table 3: Concrete properties

Passive Reinforcement	$E_s =$	$200000MPa$
	$E_p =$	$20MPa$
	$f_y =$	$550MPa$
Active Reinforcement	$E_s =$	$190000MPa$
	$E_p =$	$0MPa$
	$f_y =$	$1690MPa$
	$f_{pu} =$	$1860MPa$

Table 4: Reinforcement properties

The load applied by the hydraulic jack was hold at the different load levels and loading-unloading cycles were made before the load was increased monotonically until failure that was registered at 412 KN in the hydraulic jack that corresponds to a shear effort of 313 KN in the

analyzed section. The cracking started with vertical cracks due to bending near the point of application of the load with the increment of the load cracks turned and inclined propagation took place. The tested beam presented a shear failure mode with the corresponding yielding process of the stirrups and diagonal cracking.

The ultimate numerical load is obtained as the predicted maximum shear force obtained by TINSA plus the vertical component of the prestress force.

$$V_U = V_{TINSA} + P_{WIRE} \sin \alpha = 377KN \tag{57}$$

This value is a 20% higher than the experimental one. A better prediction can be made adjusting the dilatancy parameter, but is an improvement compared with other constitutive models that predicted ultimate forces 38% higher than the experimental value.

Figure (18) presents the numerical moment-curvature curve and the shear-generalized shear deformation curve obtained with TINSA. It can be seen that the response presents a softening in shear and a snap back in the moment curvature-curve.

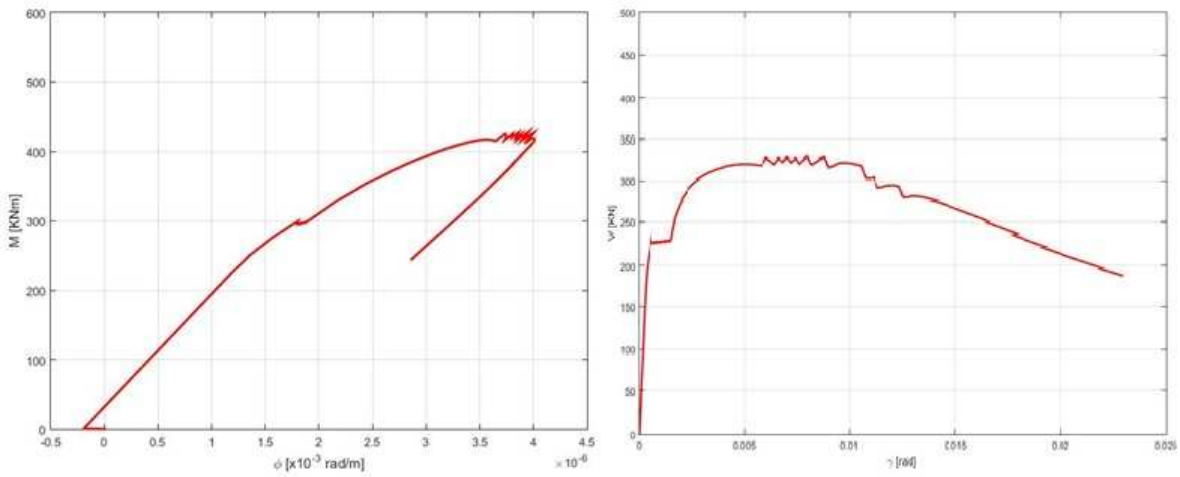

Figure 18: Numerical $M - \phi$ - Numerical $V - \gamma$

Figure (19) presents the evolution of the tension damage variable for different load levels. The cracking appears at the web of the cross-section and as load increases the damage is propagated in the web. At the ultimate load level it can be seen that the damage is concentrated in the web of the section which is completely damaged and the head remains with no damage. This numerical prediction corresponds with the experimental behavior because cracking in the analyzed section is a diagonal cracking that affects the web of the cross section and at the end of the tests no crack was identified at the head of the beam.

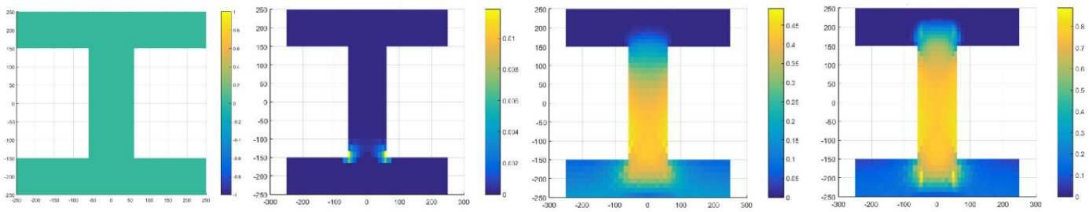

Figure 19: Evolution of the tension damage variable κ_t

Figs. (20) and (21) presents the distribution of the stresses at different load levels. At early stages the distribution of the axial stress is linear and the tangential stress xz is parabolic in the web of the beam as can be predicted by classical theories. Once cracking begins a redistribution takes place and at the end of the test it can be seen that only the head has axial stresses and is the only part of the concrete section that still resists.

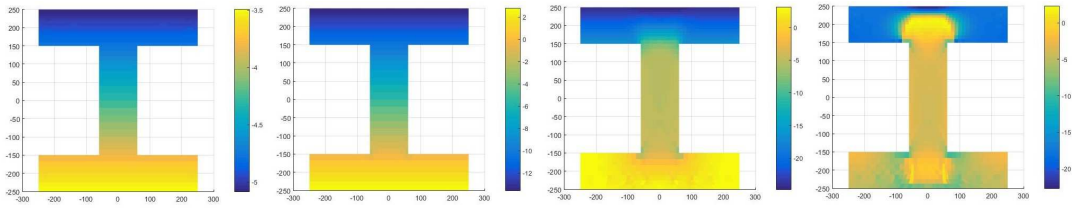

Figure 20: Evolution of σ_x distribution

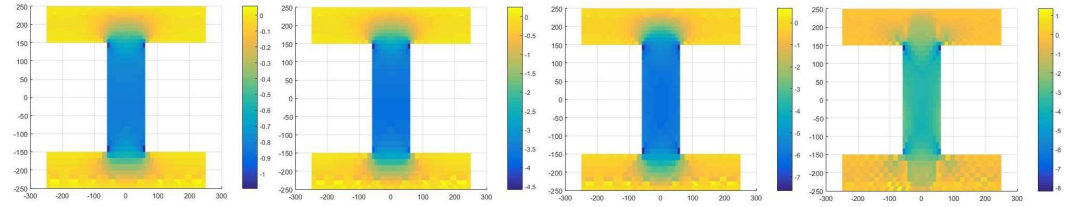

Figure 21: Evolution of τ_{xz} distribution

Figs. (22) and (23) shows the evolution of the stresses in the stirrups and the plastic deformation respectively. For low load levels the transverse reinforcement steel behaves linearly and after cracking and redistribution the portion of the shear forces resisted by the stirrups increases. Finally it can be seen that plastic deformation of the stirrups begins in the vertical bars and is extended to almost the total length of the stirrup at the end of the test. This behavior is coincident with the one observed in the experiment.

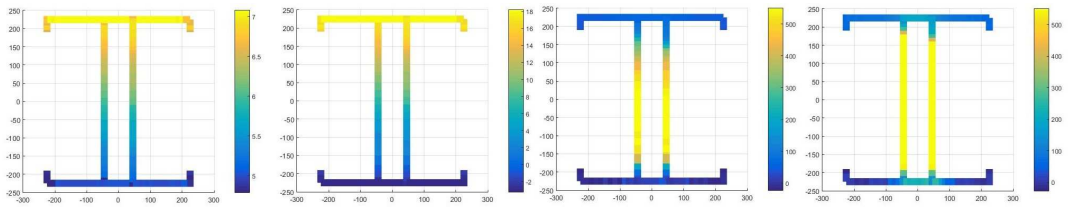

Figure 22: Evolution of stresses in the stirrups

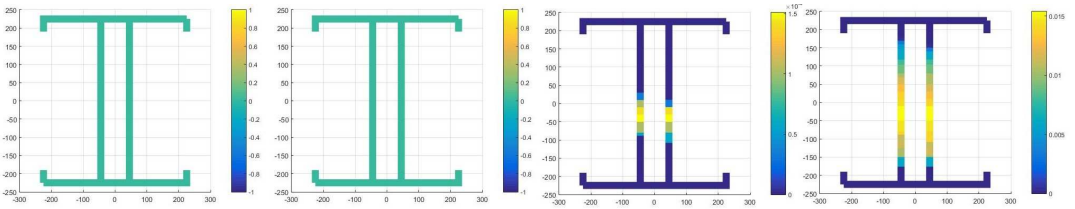

Figure 23: Evolution of plastic deformation in the stirrups

The test presented shows the usefulness of TINSA in the analysis of reinforced concrete sections under complex load states, it can reproduce the shear failure mode that most of classical beam models are not capable to do. Also the plastic-damage model used as constitutive law has a good agreement with the experimental result in spite that it can be improved by a better calibration of the material parameters.

6 CONCLUSIONS

The sectional model presented is able to reproduce the total interaction between the different efforts that takes place in beams under complex load states and with complex material behavior as reinforced concrete frame structures. This is done by considering the full set of equilibrium equations differently from classical beam formulations which neglect the inter-fiber equilibrium. The decomposition of the problem into the structural level and sectional level allows the sectional model to be independent of the frame formulation and can be used as a constitutive equation on each integration point of the beam.

In order to improve the capabilities of the sectional model a thermodynamically consistent constitutive law for concrete was implemented and presented. This law, based in classical plasticity theory, introduces a new yield surface which has as hardening variables two scalar variables defined by means of the fracture-energy damage concept. Stiffness degradation is considered uncoupled of the elastoplastic response which allows a simple numerical implementation. Also a non-associative flow rule is used to match experimental data.

A unified library of nonlinear solvers was introduced and implemented in the FE code to allow the analysis of highly nonlinear problems. This unified library enables the implementation of several control methods by means of a general constraint equation. Four control methods were implemented. This library allows the user to choose the control method that best suits the problem to be analyzed, also more than one method can be used during a single analysis which improves the convergence and the speed of the process.

The FE code with the new plastic-damage constitutive model and the unified library of nonlinear solvers was tested with two application examples. First a simple analysis of the moment-curvature response of a rectangular reinforced concrete section with different concomitant shear force was made. This example shows the influence of the concomitant shear force, which produces a reduction in the yielding moment, it also modifies the ductility of the section and the stiffness of the section. This phenomenon cannot be reproduced with most of classical beam elements. Finally a complex double-T prestressed reinforced concrete section was analyzed and numerical response was compared with experimental results, good agreement was achieved by means of the presented model, and complex behavior was predicted, shear failure was captured and the damage field corresponded to the cracking path observed in the experiment, also the contribution and behavior of the compression head was captured which is very important when the web is fully damaged but the section still resist thanks to compression head.

Further work can be done to improve the presented model . In regards to the TINSA model an improvement of the plane-section hypothesis can be made allowing the definition of subsections that can act independently of the rest of the section, this will allow the model to concentrate curvatures in just one part of the section, this improvement comes from experimental observations of T and double-T sections where the head acts as an independent beam after the web reached a full damage state. When it comes to the constitutive law and its implementation a better tangent stiffness matrix can be implemented to improve the convergence of the plastic-damage constitutive law, also the dilatancy control can be modified to better suit experimental data. Finally, in regards to the nonlinear library, new control methods can be implemented to

offer other possibilities to the user when it comes to control of the nonlinear solution process.

7 ACKNOWLEDGMENTS

This work has been carried out in the context of the master thesis presented by the first author as partial fulfillment of the requirements to obtain the degree of Master in Engineering Science of the *Université Pierre et Marie Curie* and *École Nationale des Ponts et Chaussées*, France. This thesis was carried at *Departament D'Enginyeria de la Construcció, Universitat Politècnica de Catalunya* under the supervision of professor Jesús Bairán. The firs author express his gratitude to the scholarship program *BECAR* of the Argentinian Government for the financial support and to professors Bairán,J. and Oller, S. for their valuable suggestions and comments.

REFERENCES

Bairán J. *A non-linear coupled model for the analysis of reinforced concrete sections under bending, shear, torsion and axial forces*. Ph.D. thesis, Departament D'Enginyeria de la Construcció, Universitat Politècnica de Catalunya, Barcelona, 2005.

Bairán J. and Marí A. Coupled model for the non-linear analysis of anisotropic sections subjected to general 3d loading. part 1: Theoretical formulation. *Computers & Structures*, 84:2254–2263, 2006a.

Bairán J. and Marí A. Coupled model for the non-linear analysis of anisotropic sections subjected to general 3d loading. part 2: Implementation and validation. *Computers & Structures*, 84:2264–2276, 2006b.

Bazant Z. Instability, ductility and size effect in strain-softening concrete. *J. Eng. Mech. ASCE*, 102(2):331–344, 1976.

Bazant Z. Coment on orthotropic models for concrete and geomaterials. *J. Eng. Mech. ASCE*, 109:849–865, 1983.

Lee J. and Fenves G. Plastic-damage model for cyclic loading of concrete structures. *Journal of Engineering Mechanics*, 124(8):892–900, 1998.

Lee J. and Fenves G. A return-mapping algorithm for plastic-damage models: 3d plane stress formulation. *International Journal for Numerical Methods in Engineering*, 50:487–505, 2001.

Leon S., Paulino G., Pereira A., Menezes I., and Lages E. A unified library of nonlinear solution schemes. *Applied Mechanics Review*, 64, 2011.

Lubliner J., Oliver J., Oller S., and Oñate E. A plastic-damage model for concrete. *Int. J. Solids Structures*, 25(3):299–326, 1989.

Möller O., Quiroz L., and Rubinstein M. Desempeño numérico de elementos de barra en análisis no lineal estático y dinámico. *Mecánica Computacional, AMCA*, XXVIII:587–611, 2009.

Oliver J. A consistent characteristic lenght for smeared cracking models. *International Journal for Numerical Methods in Engineering*, 28:461–474, 1989.

Omidi O. and Lofti V. Finite element analysis of concrete structures using plastic-damage model in 3d implementation. *Ing. J. Civil Engineering*, 8(3):187–203, 2010.

Poliotti M., Möller O., and Ascheri J. Modelo numérico de elemento de barras discretizado en fibras para columnas sismorresistentes. *Mecánica Computacional, AMCA*, XXXII:807–827, 2013.

Taucer F., Spacone E., and Filippou F. A fiber beam-column element for seismic response analysis of reinforced concrete structures. *Earthquake Engineering Research Center*, Report EERC 91-17, 1991.